J|A|C|S
JOURNAL OF THE AMERICAN CHEMICAL SOCIETY

Article
pubs.acs.org/JACS

Protic Ionic Liquids as p-Dopant for Organic Hole Transporting Materials and Their Application in High Efficiency Hybrid Solar Cells

Antonio Abate,[†] Derek J. Hollman,[†] Joël Teuscher,[†,#] Sandeep Pathak,[†] Roberto Avolio,[§]
Gerardino D'Errico,[∥] Giuseppe Vitiello,[∥] Simona Fantacci,[⊥] and Henry J. Snaith*,[†]

[†]Clarendon Laboratory, Department of Physics, University of Oxford, Parks Road, Oxford, OX1 3PU, United Kingdom

[§]Institute of Polymer Chemistry and Technology (ICTP), National Research Council of Italy, Via Campi Flegrei 34, 80078 Pozzuoli (NA), Italy

[∥]Department of Chemical sciences, University of Naples "Federico II", Via Cinthia, 80126 Napoli, Italy

[⊥]Computational Laboratory for Hybrid/Organic Photovoltaics (CLHYO), via Elce di Sotto 8, I-06213 Perugia, Italy

Supporting Information

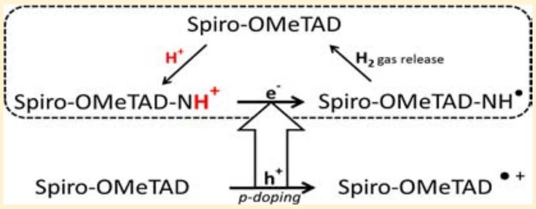

ABSTRACT: Chemical doping is a powerful method to improve the charge transport and to control the conductivity in organic semiconductors (OSs) for a wide range of electronic devices. We demonstrate protic ionic liquids (PILs) as effective p-dopant in both polymeric and small molecule OSs. In particular, we show that PILs promote single electron oxidation, which increases the hole concentration in the semiconducting film. The illustrated PIL-doping mechanism is compatible with materials processed by solution and is stable in air. We report the use of PIL-doping in hybrid solar cells based on triarylamine hole transporting materials, such as 2,2′,7,7′-tetrakis(*N*,*N*-di-*p*-methoxyphenyl-amine)9,9′-spirobifluorene (spiro-OMeTAD). We show improved power conversion efficiency by replacing lithium salts, typical p-dopants for spiro-OMeTAD, with PILs. We use photovoltage−photocurrent decay and photoinduced absorption spectroscopy to establish that significantly improved device performance is mainly due to reduced charge transport resistance in the hole-transporting layer, as potentiated by PIL-doping.

■ INTRODUCTION

Organic semiconductors (OSs) are entering the electronics market in various stages of development for a range of applications and are expected to grow significantly in the near future. Key factors driving penetration of organic electronics in the mainstream market are their low cost of fabrication and their high degree of flexibility.[1] Since their discovery in 1977,[2] several studies have shown the possibility of tuning their properties for specific applications by chemical doping.[3] Chemical doping may be achieved by introducing "impurities" into the OSs, which increases the density of mobile charge carriers and thus conductivity; through this, doped organic semiconductors operate similarly to traditional inorganic semiconductors. In practice, chemical doping can involve several mechanisms depending on both the semiconductor and the dopant.[3] Doping of polyacetylene via protonation was the primary chemical doping achieved by immersion of polyacetylene in aqueous HCl.[4] Upon drying the polymer, residual H_3O^+ groups remain within the organic matrix, increasing the density of mobile charges by inductively withdrawing electrons from the electron-rich conjugated polymer chains; the resulting p-doped OS showed an increase in conductivity of 10 orders of magnitude.[4] Following this study, aqueous H^+ treatment of OSs has been reported as a general doping mechanism for many conjugated polymers.[5−9] Recently, several heterocyclic organic hydrides[10] have been reported as efficient n-type dopants by releasing hydride (H^-) or atomic hydrogen ($H^\bullet$).[11] In particular, 1,3-dimethyl-2-phenyl-2,3-dihydro-1H-benzoimidazole derivatives (DMBI) can increase the conductivity of [6,6]-phenyl C61 butyric acid methyl ester (PCBM) by more than 4 orders of magnitude through this chemical doping treatment.[11] Following $H^\bullet$ release, highly energetic DMBI radicals reduce PCBM, increasing the density of mobile charge carriers in the OS matrix. The stability of this doping mechanism depends on the rate of the back electron transfer from the doped PCBM to the DMBI cation, which can be stabilized by an electron-rich substituent on DMBI core.[12] This mechanism has been effectively applied to prepare air-stable organic thin-film transistors.[12] Many other organic electronic applications can benefit from chemical doping; for example, triphenylamine-based OSs have been p-doped with Co(III) complexes in solar cells[13] and tetracyano-quinoline derivatives in organic light-emitting diodes.[14] Both systems benefit from the introduction of a p-doped transport layer, reducing the charge transport series resistance with the photoactive junction[13,15−17] and helping to forge ohmic contacts at the electrode interfaces.[18−20] Furthermore, chemical doping may also facilitate the fabrication of tandem structures for efficient organic solar cells using a versatile recombination contact.[21]

Received: June 20, 2013
Published: July 25, 2013

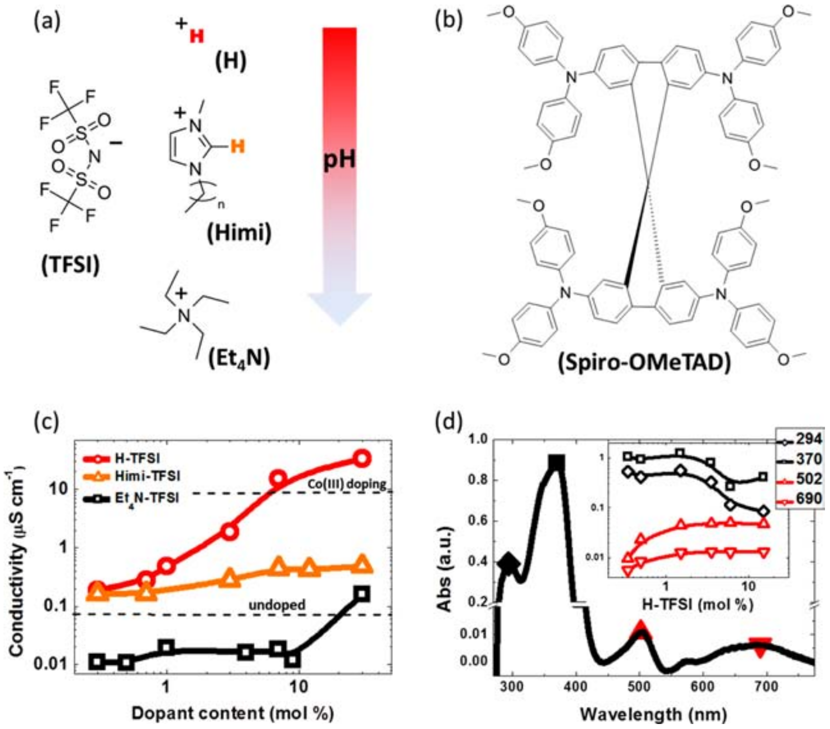

Figure 1. (a) Chemical structure of ionic liquids used in this study: H-TFSI and Himi-TFSI ($n = 5$ for the data reported in this work) are PILs, with H-TFSI more acidic (free proton in red) than Himi-TFSI (the most acidic proton in orange),[22] and Et_4N-TFSI as an aprotic ionic liquid. The pH scale may be considered as an indication of how strongly a proton will be transferred from the PIL to a base, though it must be noted that the pH is usually considered for aqueous solutions and may not be appropriate for the nonaqueous PILs. (b) Chemical structure of the small molecule organic semiconductor used in this study, spiro-OMeTAD. (c) Conductivity against the content of different ionic liquids; the dashed lines indicate the conductivity of the undoped and the Co(III)-doped[13] spiro-OMeTAD as measured in our laboratory. (d) UV−vis absorption spectra of spiro-OMeTAD doped with H-TFSI and the absorption intensity at specific wavelengths as a function of the H-TFSI concentration (inset). Peaks at 502 and 690 nm have been assigned to oxidized spiro-OMeTAD (spiro-OMeTAD$^+$ or spiro-OMeTAD^{2+}).[33]

However, most of the dopants reported in scientific literature have never been exploited for electronic applications since their application was incompatible with cost-effective processing or their doping effects were weak and reversible during the device operation.

In this work, we report the use of protic ionic liquids (PILs)[22] as a protonation generator to describe a new, efficient, and air-stable p-doping mechanism. We show that PILs, used as a source of H^+, are effective dopants in small molecule OSs.[5−8,23] We report both experimental and theoretical analyses to establish a PIL-doping mechanism in OSs. In particular, we show that bis(trifluoromethanesulfonyl)imide (H-TFSI), as source of H^+, increases the conductivity of 2,2′,7,7′-tetrakis(*N*,*N*-di-*p*-methoxyphenyl-amine)9,9′-spirobifluorene (spiro-OMeTAD) by 3 orders of magnitude. Additionally, we take advantage of PIL-doping to demonstrate solid-state dye-sensitized solar cells (ss-DSSCs)[24] and meso-superstructured solar cells (MSSCs)[25,26] with improved photon to electron power conversion efficiency compared to the state-of-the-art. We use photovoltage−photocurrent decay and photoinduced absorption spectroscopy (PIA) to establish that significantly improved device performance is mainly due to reduced charge transport resistance in the hole-transporting matrix, as potentiated by PIL-doping.

■ RESULTS AND DISCUSSION

Recently, numerous studies have focused on ionic liquids both as solvents and as electrolytes for electronic applications.[27] This interest is due to their remarkable properties, such as negligible vapor pressures, low melting points, nonflammability, and a significant ability to solvate many organic and inorganic chemicals.[28] In the broad range of ionic liquids, PILs are Brønsted acid−base combinations, wherein the proton transfer from acid to base creates the anion−cation couple.[22] The archetypal PIL is bis(trifluoromethane)sulfonimide (H-TFSI, see Figure 1a), in which the cation is H^+ and the anion is CF_3SO_2-N^--SO_2CF_3. In this particular anion, the extremely electron-withdrawing CF_3SO_2- groups reduce the basic character of the imide nitrogen (-N-), distributing the negative charge over multiple atoms.[29] As a consequence of this, the self-dissociation of H-TFSI produces "free" protons in organic solution, similarly to an aqueous HCl solution.[30] Thus, organic molecules dissolved in H-TFSI solutions have a high probability of being protonated, and stable organic cations may be generated, coupled with a TFSI anion.[22] The rate of proton transfer can be controlled by tuning the acidic character of PIL.[30] Indeed, in addition to H-TFSI, several N-heterocyclic ionic liquids may be used as weak Brønsted acids.[31] In particular, 1-alkyl-3-methylimidazolium bis(trifluoromethane)-sulfonimide (Himi-TFSI, see Figure 1a) has been shown to produce stable carbenes by means of proton release from the aromatic ring.[32] Nevertheless, the self-dissociation constant for Himi-TFSI is much lower than H-TFSI, as symbolically indicated on the pH scale in Figure 1a.[30] Also in Figure 1a, we reported an aprotic ionic liquid, tetraethyl bis-(trifluoromethane)sulfonimide (Et_4N-TFSI), which can be assigned as a weak Brønsted base.

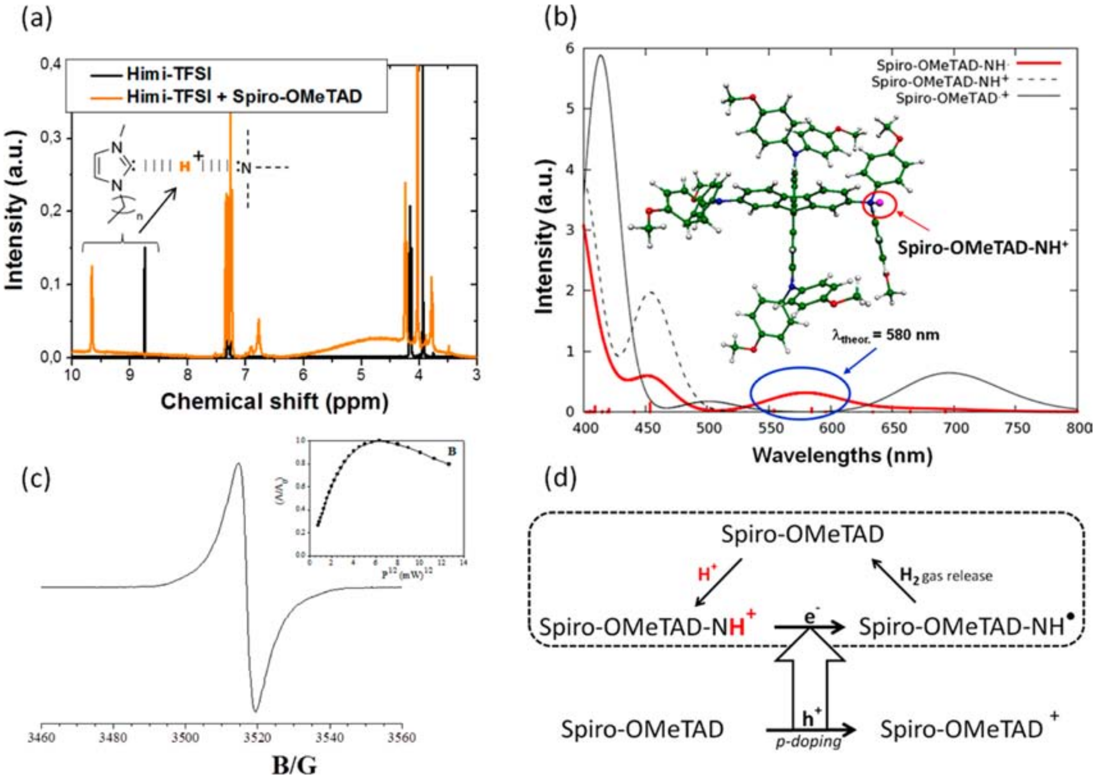

Figure 2. (a) ^{1}H NMR collected in deuterated dimethyl sulfoxide for Himi-TFSI and for spiro-OMeTAD doped with Himi-TFSI shows a strong downfield shift of the peak belonging to the most acidic hydrogen atom (highlight in Figure 1a) of the imidazolium cation from 8.7 to 9.7 ppm, which is indicative of interaction with a Lewis base. (b) TDDFT computed absorption spectra of the spiro-OMeTAD protonated on nitrogen (spiro-OMeTAD-NH$^+$, black dashed line), the reduced species of the protonated spiro-OMeTAD (spiro-OMeTAD-NH$^\bullet$ red line), and the oxidized spiro-OMeTAD (spiro-OMeTAD$^+$ black solid line). The DFT optimized geometry of spiro-OMeTAD-NH; the added proton is colored purple and is encircled with red. Spectral absorption band of the spiro-OMeTAD-NH species has been highlighted blue and the TDDFT excitations reported. (c) EPR spectrum and influence of microwave power on spectrum amplitude of H-TFSI-doped spiro-OMeTAD powder. (d) Proposed scheme of PIL-doping mechanism.

To demonstrate the p-doping effect of PILs, we focus our experiments on the well-known small molecule OS, spiro-OMeTAD (see Figure 1b), a state-of-the-art organic hole transporting material in hybrid solar cells.[13,25] However, recent studies have demonstrated that the slow charge transport and the ensuing low conductivity of spiro-OMeTAD significantly limit the power conversion efficiency (PCE) of solar cells fabricated with this hole transporting material.[34] Indeed, Burschka and co-workers significantly enhanced the PCE in ss-DSSCs by using Co(III) complexes as a chemical dopant, increasing the conductivity of spiro-OMeTAD by 2 orders of magnitude.[13]

PIL-Doping Mechanism. In Figure 1c we reported the conductivity of spiro-OMeTAD as function of the ionic liquid content, as measured in inert atmosphere (nitrogen) and dark condition. A fast growth in conductivity with doping concentration is immediately visible for both H-TFSI and Himi-TFSI at low concentration, which reaches a plateau around 10 mol % with spiro-OMeTAD. Notably, H-TFSI can enhance the conductivity by up to 3 orders of magnitude compared to the undoped OS. Et_4N-TFSI shows that the addition of aprotic ionic liquids in the organic matrix has a detrimental effect on the conductivity. We should nevertheless note the increase in conductivity at very high concentration of Et_4N-TFSI (30 mol % with spiro-OMeTAD). This effect, which can occur regardless the presence of “free” proton, could be attributed to the electrostatic charge of the ionic species added into the organic matrix, as discussed in previous reports.[35] However, to prove the diverse nature of doping with protic and aprotic ionic liquids, in Figure 1d we report the UV−vis absorption spectra for the spiro-OMeTAD films doped with H-TFSI. There is a clear growth of absorption bands at 502 and 690 nm and a simultaneous decrease of the bands at 294 nm and at 370 nm, as the concentration of H-TFSI is increased. As already observed for the conductivity, the absorption changes very rapidly at low H-TFSI content, reaching a plateau around 10 mol %. A clear trend for Himi-TFSI-doped films could not be obtained, since the absorption at 510 and 690 nm was too weak (see Supporting Information, SI). The same spectra for Et_4N-TFSI showed only the bands at 294 and 370 nm without any indication of absorption at both 510 and 690 nm, even with high dopant concentration. These absorption modes in the spiro-OMeTAD have already been assigned via experimental and computational studies to the neutral molecule (spiro-OMeTAD, 294 and 370 nm) and first or second oxidized state (spiro-OMeTAD$^+$ or spiro-OMeTAD^{2+}, 502 and 690 nm).[24,33,34] Thus, we have evidence that PILs can oxidize (p-dope) spiro-OMeTAD depending on their ability to release protons. We also note a weak absorption band at 575 nm, which has not been previously observed in oxidized spiro-OMeTAD,[33,34] and it may therefore belong to new species generated by PIL doping, which we will investigate below.

To shed light on the PIL-doping mechanism, we first demonstrate the protonation of spiro-OMeTAD through measuring ^{1}H NMR spectra (Figure 2a). While the spectrum of spiro-OMeTAD in deuterated dimethyl sulfoxide gives sharp peaks (see SI), upon addition of PILs to the solution, most of the peaks become deformed, substantially broadened, or completely quenched. This may be due to paramagnetic radical species generated after the addition of PIL, such as the formation of spiro-OMeTAD$^+$ that we described in Figure 1d. Particularly, when we added a strong acidic PIL, such as H-TFSI, no signals from spiro-OMeTAD could be measured (the TFSI ion does not contain hydrogen), while a weaker acidic PIL, such as Himi-TFSI, still allowed the identification of the collapsed peaks at 3.7, 6.8, and 6.9 ppm along with the spectrum of Himi$^+$ (see Experimental Section for more details). The persistence of PIL ^{1}H resonances suggests that the quenching of the signals for spiro-OMeTAD is not solely due to the fast-relaxation effect of paramagnetic species in solution.[36] Indeed, in this case we should see a similar deformation for the resonances of the entire spectrum rather than specifically for spiro-OMeTAD.[36] As previously reported,[37−39] such specific quenching may be ascribed to one-electron oxidation of the protonated molecule, which generates paramagnetic radical species in addition to spiro-OMeTAD$^+$.[40] However, radical species may also strongly deform the ^{1}H signals of the remaining molecules in solution, depending on their relative concentration.[37] Subsequently, in order to reduce the concentration of the radical species, we focus our ^{1}H NMR experiments on Himi-TFSI, which is a significantly weaker acid than H-TFSI (see Figure 1). In Figure 2a we report the spectra for Himi-TFSI in the presence and absence of spiro-OMeTAD to demonstrate the proton-exchange reaction. The peak of the most acidic hydrogen atom, highlighted in Figure 1a, showed a strong downfield shift, from 8.75 to 9.66 ppm upon addition of spiro-OMeTAD.[41] Notably, the remaining peaks from both Himi-TFSI and spiro-OMeTAD remained unaffected, as detailed in the Experimental Section. Such behavior is compatible with a partial or a complete proton transfer from the imidazolium cation to a basic site of the spiro-OMeTAD.[41] The possible basic centers of the spiro-OMeTAD are the triphenylamine nitrogens and the etheric oxygens. We performed density functional theory (DFT) calculations to extract the stability of the structures with one proton alternatively bound to nitrogen or to oxygen centers. The species protonated on nitrogen atom (Figure 2b), hereafter labeled as spiro-OMeTAD-NH$^+$, is markedly stabler than the species protonated on an oxygen atom by as much as 20.35 kcal/mol. The optimized structures of both the protonated species and the relative formation energies are reported in the SI. As hypothesized, protonation occurs on the most basic center of the system, although the nitrogen atoms are quite sterically congested, while the oxygen sites are more accessible.

Time-dependent DFT (TDDFT) calculations were previously shown to accurately simulate the absorption spectra of the neutral spiro-OMeTAD and its oxidized species.[33] Here, we computed the spectra of spiro-OMeTAD-NH$^+$ and the possible related reduced species, i.e., the neutral spiro-OMeTAD-NH radical (spiro-OMeTAD-NH$^\bullet$, Figure 2b). In particular, the computed UV−vis spectrum of spiro-OMeTAD-NH$^\bullet$ shows a pronounced spectral feature at 580 nm, which can be related to the experimental feature found at 575 nm. It notably appears in a spectral region where the possible species that could be produced along with spiro-OMeTAD-NH$^\bullet$ are lacking any significant absorption. We can therefore assign the weak experimental absorption band at 575 nm (Figure 1d) to spiro-OMeTAD-NH$^\bullet$.

In order to probe the paramagnetic species generated by the PIL-doping, we performed electron paramagnetic resonance (EPR) on neat and PIL-doped spiro-OMeTAD, as described in the Experimental Section. The EPR spectrum of the undoped spiro-OMeTAD (see SI) shows a weak, symmetric signal due the presence of a small amount of spiro-OMeTAD$^+$, which is predictably generated by exposure to oxygen.[33,34] Otherwise, the spectrum of the PIL-doped spiro-OMeTAD is more intense and slightly asymmetric, which suggests the superposition of multiple bands due to various paramagnetic species (i.e., spiro-OMeTAD$^+$ and spiro-OMeTAD-NH$^\bullet$).[42] Furthermore, the amplitude of the EPR spectra as a function of microwave power, shown in the inset of Figure 2c, reveals a slow decrease of signal amplitude after the maximum value is reached. This heterogeneity in the power saturation profile is compatible with the presence of additional radical species together with spiro-OMeTAD$^+$. Indeed, protonated organic cations (spiro-OMeTAD-NH$^+$) can promote a single electron transfer from the parent neutral molecule (spiro-OMeTAD) to the protonated molecule via radical formation (spiro-OMeTAD$^+$ and spiro-OMeTAD-NH$^\bullet$, Figure 2d).[40,43] We highlight here that in this particular system, the electron transfer is not spontaneous, as it needs to be thermally activated, described in the Experimental Section. Then, even if we can still probe spiro-OMeTAD-NH$^\bullet$ in the OS film (absorption at 575 nm in Figure 1d), this species could spontaneously react to release hydrogen gas and regenerate neutral spiro-OMeTAD.[11] In Figure 2d, we summarize in a scheme the proposed PIL-doping mechanism. Notably, the mechanism requires two interacting spiro-OMeTAD molecules.

PIL-Doping Application in DSSCs. To demonstrate the applicability of the PIL-doping mechanism, we prepared ss-DSSCs and perovskite-based MSSCs utilizing spiro-OMeTAD as the organic hole transporting layer. The state-of-the art ss-DSSCs and MSSCs are assembled using lithium bis(trifluoromethylsulfonyl)-imide (Li-TFSI) and 4-*tert*-butylpyridine (*t*BP) as additives to spiro-OMeTAD.[13,44,45] The lithium ion (Li$^+$) has been reported as essential for device operation since it helps lower the device series resistance (R_s) and enhances photocurrent generation.[46,47] We recently demonstrated that the lowering of the R_s is mainly due to an effective p-doping of the organic hole transporter, which can be activated by Li$^+$ only in presence of oxygen (Li-doping).[34,48] However, we also showed that despite the Li-doping, the device power conversion efficiency is still significantly limited by R_s.[34] Indeed, Burschka and co-workers were able to significantly enhance the device performance by simply introducing another p-dopant, in addition to Li-TFSI, to improve the conductivity of the hole transporting layer.[13] Here, we demonstrate that replacing Li-TFSI with PIL-doping in spiro-OMeTAD decreases R_s, thus improving PCE. We first focus on ss-DSSCs, where the additives (Li-TFSI and *t*BP; or PILs) must be carefully investigated, since they affect not only the charge transport in the hole transporter but also the electron transport in the TiO_2 as well as the charge recombination at TiO_2/spiro-OMeTAD interface. The ss-DSSCs have been prepared according to the procedure reported in the Experimental Section, using D102 dye to sensitize the TiO_2.[49,50]

To quantify the influence of PILs on the device operation, we performed transient photovoltage−photocurrent decay measurements on PILs and Li-TFSI based ss-DSSCs.[51] From now,

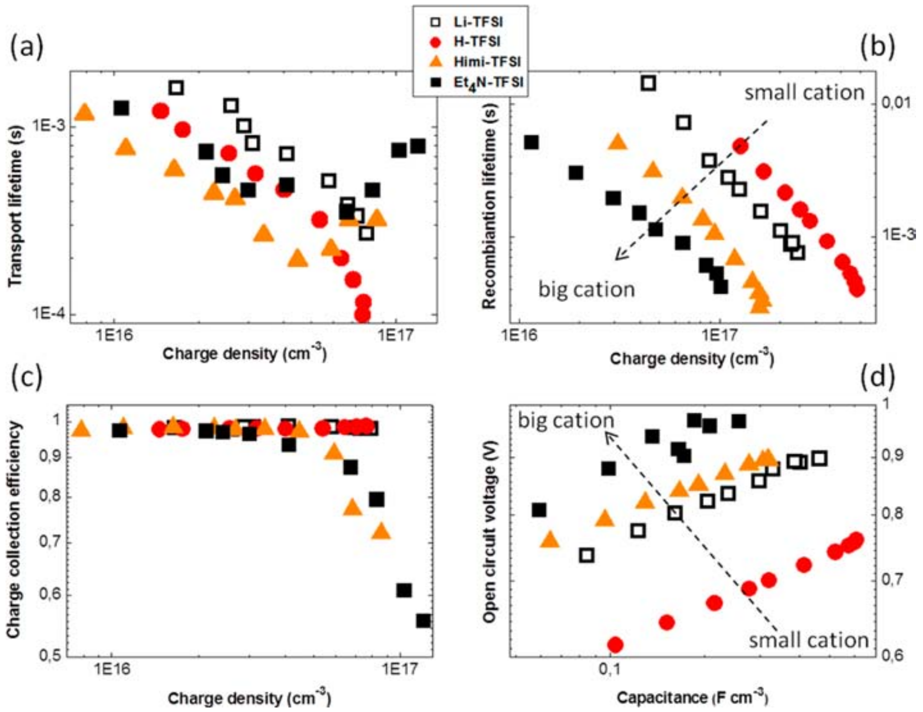

Figure 3. Charge transport, recombination, collection efficiency, and capacitance from photovoltage−current decay measurements[51] for devices prepared with PILs and Li-TFSI. (a) Transport lifetimes at short circuit conditions (τ_{trans}) against charge density at short circuit. (b) Recombination lifetimes at open circuit conditions (τ_{rec}) against charge density at open circuit. (c) Charge collection efficiency (η_{col}) against charge density at short circuit. (d) Open circuit voltage against the differential capacitance.

we will be using the name of the salt (PIL and Li-TFSI) to denote the full device incorporating the salt. From these measurements, it is possible to extract the capacitance in the TiO_2, recombination lifetime (τ_{rec}), charge transport lifetime (τ_{trans}), and charge collection efficiency (η_{col}).[51,52] In Figure 3a we show that τ_{trans} monotonically decreases with charge density for Li-TFSI and H-TFSI, while Himi-TFSI and Et$_4$N-TFSI seem to limit the charge transport at high charge density. To explain this trend, we should consider that at low charge densities ($\sim 1 \times 10^{16}$ cm^{-3}), the electron transport in the TiO_2, rather than hole transport in the spiro-OMeTAD, is limiting charge transport, this effect being similar for each dopant used.[53] As the charge density increases ($>1 \times 10^{17}$ cm^{-3}), the electron transport rate in the TiO_2 becomes comparable to the hole transport in the spiro-OMeTAD.[54] In this regime, the hole transport can limit the charge transport if the spiro-OMeTAD is insufficiently doped.[34,55] Therefore, Himi-TFSI and Et$_4$N-TFSI are, effectively, limiting the charge transport for charge densities above 1×10^{17} cm^{-3}, which is the standard operating range for devices.[34] In Figure 3b we show that τ_{rec} follows the same trend with charge density for each dopant. At the same charge density, τ_{rec} increases as the cation hydrodynamic volume decreases ($Et_4N^+ > Himi^+ > Li^+ > H^+$).[56] A similar effect has been previously observed for liquid electrolyte DSSCs.[57−59] The recombination trend with the cation volume can be explained by the relative ability of different positive ions to penetrate the dye layer and approach the TiO_2 surface.[46,60] Though the volumes of Et_4N^+ and $Himi^+$ are comparable (depending on the surrounding molecules), $Himi^+$ is expected to be considerably more compatible with the hydrophilic TiO_2 surface than Et_4N^+.[27] From the measurement of τ_{trans} and τ_{rec}, we can extract the η_{col} as the ratio of the transport rate constant (inverse of lifetime) over the sum of transport and recombination rate constants.[52] Figure 3c shows η_{col} remains constant with increasing charge density for Li-TFSI and H-TFSI, indicating that the faster charge transport compensates for the increased recombination as charge density increases. For Himi-TFSI and Et$_4$N-TFSI, the same increase in recombination is not compensated by faster transport, which thus limits η_{col} at higher light intensities. In Figure 3d we show the open circuit voltage (V_{oc}) as a function of the differential capacitance in the TiO_2.[51] All the curves follow a similar trend, which suggests that the dopants used in this work leave the density of states distribution below the TiO_2 conduction band unchanged.[34,46,61−63] Therefore, any differences in V_{oc} may be directly related to a shift in the relative position between the quasi-Fermi level for the electrons in TiO_2 and the holes in spiro-OMeTAD. Cappel and co-workers demonstrated that this energy alignment depends on the dipole moment augmented at the TiO_2 interface.[64] In our system, the interfacial dipole may be affected by the ability of the positive ion to penetrate the dye layer and approach the TiO_2. Indeed, at the same capacitance, V_{oc} decreases as the cation hydrodynamic volume decreases ($Et_4N^+ > Himi^+ > Li^+ > H^+$).

To demonstrate the impact of these parameters on power conversion efficiency, we report in Figure 4 the characteristic current−voltage (J−V) curves for the same devices. Each characteristic has been measured under AM1.5 simulated sun light of 100 mW cm^{-2} equivalent solar irradiance with shadow masking as described in the Experimental Section.[65] Table 1 lists the performance parameters for the devices reported in Figure 4 and the device series resistance as extracted by fitting J−V curves to an ideal diode model.[34]

The short circuit photocurrent density (J_{sc}) shows monotonic growth with decreasing cation size from Et$_4$N-TFSI to H-TFSI. This trend could be explained considering the

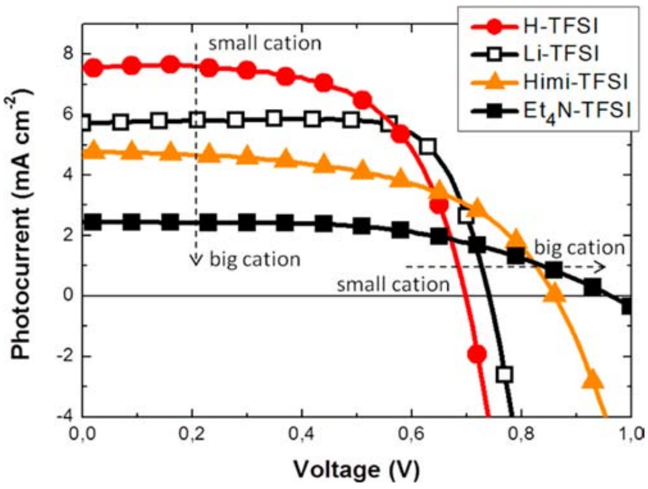

Figure 4. Photocurrent–voltage curves for devices employing different additives. All devices were sensitized with D102[49,50] and measured under AM1.5 simulated sun light of 100 mW cm^{-2} equivalent solar irradiance. All devices employed the same amount of *t*BP as described in the Experimental Section.

Table 1. Solar Cell Performance Parameters: Short Circuit Photocurrent (J_{sc}), Power Conversion Efficiency (PCE), Open Circuit Voltage (V_{oc}), Fill Factor (ff), and Series Resistances (R_s)[a]

	J_{sc} (mA cm^{-2})	PCE (%)	V_{oc} (V)	ff	R_s (Ω)
H-TFSI	7.53	3.27	0.70	0.62	43
Li-TFSI	5.70	3.16	0.74	0.75	57
Himi-TFSI	4.77	2.22	0.86	0.54	224
Et_4N-TFSI	2.44	1.26	0.96	0.54	1293

[a] As extracted by fitting *J*–*V* curves to an ideal diode model.[34]

shift of the electron Fermi level in the TiO_2 for different additives as described in Figure 3d. As widely reported in literature, a downshift of the Fermi level in the TiO_2 results in a more favorable electron injection from the dye excited state to the metal oxide.[66,67] The J_{sc} for Li-TFSI, according to the trend observed in Figure 3d, is located between Himi-TFSI and H-TFSI. For the same reason, open circuit voltage (V_{oc}) follows the opposite trend. The fill factor (ff) trend could be explained by considering both the charge recombination and the device series resistance due to the hole transport in the spiro-OMeTAD.[53] For Li-TFSI and H-TFSI, the device series resistance is similar (see Table 1), and the recombination lifetime at the same charge density is longer for H-TFSI (see Figure 3b), which helps to recover from a significant fraction of the V_{oc} loss. Himi-TFSI and Et_4N-TFSI suffer from both high recombination and series resistance, resulting in significantly diminished fill factor. The overall PCE shows that H-TFSI and Li-TFSI perform similarly, while Himi-TFSI and Et_4N-TFSI perform substandardly.

We note here that the previous devices have been prepared, according to the state-of-art ss-DSSCSs, employing *t*BP as an additive together with PILs or Li-TFSI, as described in the Experimental Section.[13,45,68] The *t*BP has been reported to raise the surface potential of the TiO_2, which partially compensates for the positive shift of Li^+ by recovering the V_{oc} and decreasing the J_{sc}.[58] The highest PCE for Li-TFSI-based devices has been achieved by tuning the relative amount of Li^+ and *t*BP in order to attain a well-balanced compromise between J_{sc} and V_{oc}.[34] In the aforementioned experiment, we used additives, both the PILs and the *t*BP, at the same concentration that has been optimized for Li-based devices. However, focusing on Himi-TFSI in particular, the substantially reduced J_{sc}, despite high $V_{oc,}$ suggests that the addition of *t*BP could be detrimental for its performance. In Figure 5, we reported the device *J*–*V* for Himi-TFSI without *t*BP compared to the optimized Li-TFSI *t*BP one. Notably, the Himi-TFSI reaches 4% efficiency, which matches the previous record reported for D102-based ss-DSSCs.[49,50] We should note that immediately after the preparation Himi-TFSI (without *t*BP) performs very close to traditional Li-TFSI *t*BP devices (see Figure 4). Then, after storing for one month, the devices in air and dark, they showed the *J*–*V* curves reported in Figure 5. This procedure allows the conductivity of the Himi-doped spiro-OMeTAD to increase considerably due to the doping effect of oxygen.[69] Indeed, the series resistances after one month, reported in Table 2, show similar values for Li-TFSI and Himi-TFSI. To elucidate the role of the Himi-TFSI as a replacement for Li-TFSI and *t*BP, we performed PIA along with TAS.[70]

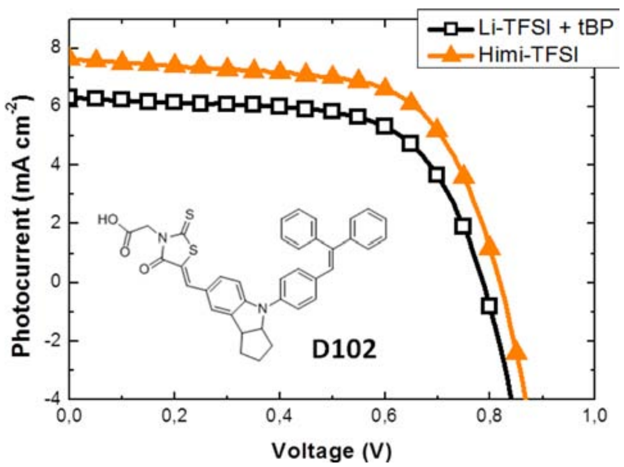

Figure 5. Photocurrent–voltage curves reported for devices employing the optimized additives composition Li-TFSI and *t*BP or Himi-TFSI. The devices were sensitized with D102[49,50] and measured under AM1.5 simulated sun light of 100 mW cm^{-2} equivalent solar irradiance after one month storarage in air and dark.

Table 2. Solar Cell Performance Parameters: J_{sc}, PCE, V_{oc}, ff, and R_s[a]

	J_{sc} (mA cm^{-2})	PCE (%)	V_{oc} (V)	ff	R_s (Ω)
Himi-TFSI (*t*BP omitted)	7.63	4.00	0.82	0.64	87
Li-TFSI + *t*BP	6.31	3.19	0.79	0.64	89

[a] As extracted by fitting *J*–*V* curves to an ideal diode model.[34]

In Figure 6a, we reported the PIA for the dye (D102)[49,50] adsorbed onto TiO_2 in the presence and absence of Li-TFSI/*t*BP and Himi-TFSI. We observe the negative feature at 570 nm due to the Stark effect[71] and two positive features at 720 and 1160 nm, which have been attributed to the oxidized dye.[70] The Stark effect is thought to arise from an electric field generated by the build-up of electrons in the TiO_2 and holes on the dye or on the spiro-OMeTAD.[70] In essence, a stronger Stark signal suggests less effective charge screening at the TiO_2 interface.[72]

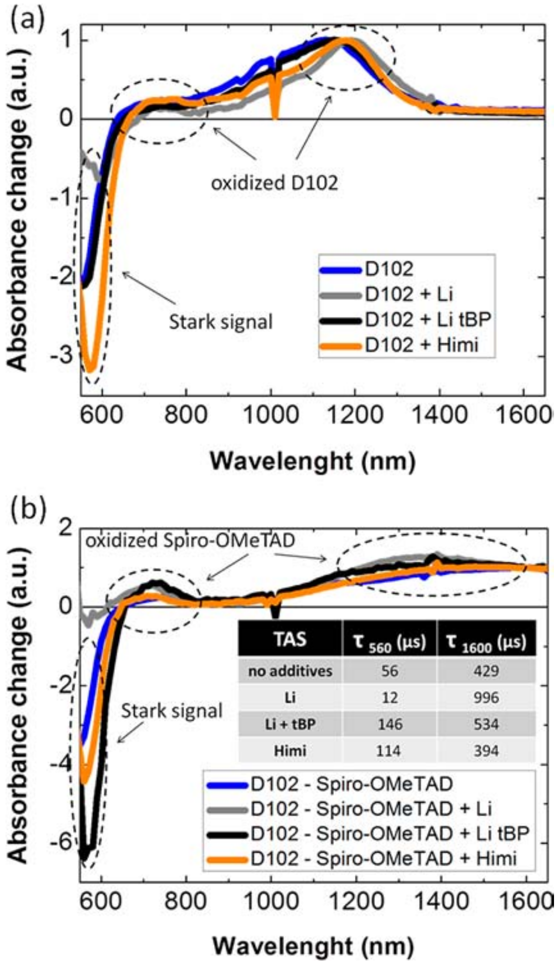

TAS	τ_{560} (μs)	τ_{1600} (μs)
no additives	56	429
Li	12	996
Li + tBP	146	534
Himi	114	394

Figure 6. (a) PIA for D102[49,50] adsorbed on TiO_2 with and without the addition of Li-TFSI, *t*BP and Himi-TFSI. (b) PIA for D102 after addition of the hole transporter with and without the addition of Li-TFSI, *t*BP, and Himi-TFSI. Inset, lifetime collected from TAS at 560 and 1600 nm on the same samples (the spectra are reported in SI).

After normalizing the curves at the same concentration of holes on the dye (1160 nm), we note a significant difference in the Stark signal amplitude between the $Himi^+$ and Li^+ (Li^+ with and without *t*BP). This could be explained by considering the diminished ability of the bulkier Himi cation to penetrate the dye layer and screen the field induced by the separated electrons and holes across the dye-sensitized interface.[57−59] In Figure 6b, we reported the same spectra collected after addition of spiro-OMeTAD. We still observe a Stark effect at 560 nm and the two positive features at 700 and 1600 nm (the latter being broad), which in this case may be attributed to oxidized spiro-OMeTAD.[47] After normalizing the spectra at the same concentration of holes on spiro-OMeTAD (1600 nm), we can see that the relative amplitude of the Stark signal (560 nm) is higher for the Li-TFSI/*t*BP system, moderate for both the Himi-TFSI system and the neat spiro-OMeTAD, and reduced to almost zero for Li-TFSI only. This trend is different from what we observed without spiro-OMeTAD (Figure 6a), where the $Himi^+$ has screened charges less effectively than Li^+. To explain this difference, we must consider that Li cations in spiro-OMeTAD film are consumed in the presence of oxygen.[34,47] After the addition of spiro-OMeTAD, their effective concentration at the TiO_2 interface could be significantly lower than previously without the spiro-OMeTAD. In addition, the *t*BP could further reduce the concentration of Li cations on the TiO_2 surface with two possible mechanisms: binding the cation via Li^+/π complexes interaction[73] or creating an organic layer on the TiO_2 surface,[74] which could reduce the ability of residual Li^+ intercalating into the metal oxide and thereby screening the injected charges. Although Himi exhibited a stronger Stark signal than Li^+, after the addition of *t*BP, the situation is reversed and the Himi-TFSI is better at screening charge.

Using transient absorbance spectroscopy (TAS), we can monitor the lifetime of the Stark features at 560 nm (τ_{560}), as reported in table inset Figure 6b. τ_{560} represents the kinetic of the screening reaction for the photogenerated charges at the TiO_2 interface.[71,72] We can see that Himi is screening charges faster (114 μs) than Li *t*BP (146 μs). Again, Li alone could screen the charge much faster (only 12 μs), but *t*BP is always needed to optimize the device performance, as previously discussed. Similarly, TAS at 1600 nm allows direct monitoring of the lifetime for the photogenerated hole in the spiro-OMeTAD (τ_{1600}). From the data reported in the table inset of Figure 6b, we can see that the holes recombine faster (shorter lifetime) for $Himi^+$ than for Li^+/*t*BP. This can be explained by considering the recombination−blocking effect of the *t*BP adsorbed onto TiO_2 surface.[44]

PIL-Doping Application in MSSCs. Lastly, we demonstrate the application of PIL-doped spiro-OMeTAD in MSSCs.[25] In this device structure the mesoporous TiO_2 is replaced by an insulating dielectric, such as Al_2O_3. The latter mesoporous metal oxide acts only as a scaffold to assist in the film formation and crystallization of the organometal halide perovskite absorber (see inset Figure 7), which generates and transports charge.[26] In this device, a thin compact layer of TiO_2 (thickness 75 nm, see SI) is nevertheless used as a selective contact for the electrons at the bottom of the active layer (thickness 400 nm, see SI).[25] Although we cannot completely exclude a direct contact between the spiro-OMeTAD and the compact TiO_2 layer,[26] the occurrence of this interface is considerably reduced compared to ss-DSSCs. This should allow the use of H-TFSI rather than Himi-TFSI as a more effective PIL-dopant without significant loss in V_{oc}, the latter of which

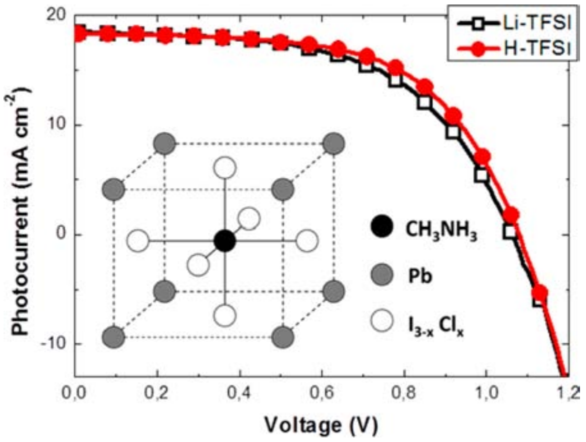

Figure 7. Photocurrent−voltage curves for devices employing Li-TFSI or H-TFSI. The devices were prepared using perovskite crystals ABX_3 (A = CH_3NH_3, B = Pb, and X = I_{3-x}, Cl_x)[25] as shown and measured under AM1.5 simulated sun light of 100 mW cm^{-2} equivalent solar irradiance.

was detrimental to maximizing the performance of ss-DSSCs (Figure 4 and Table 3).

Table 3. Solar Cell Performance Parameters: J_{sc}, PCE, V_{oc}, ff, and R_s[a]

	J_{sc} (mA cm^{-2})	PCE (%)	V_{oc} (V)	ff	R_s (Ω)
H-TFSI	18.32	11.87	1.08	0.60	87
Li-TFSI	18.29	10.86	1.06	0.56	120

[a] As extracted by fitting J−V curves to an ideal diode model.[34]

In Figure 7, we reported the device J−V curves for devices using spiro-OMeTAD doped with H-TFSI or Li-TFSI.[26] As reported in Table 2, PIL-doped devices show higher fill factor and similar V_{oc} and J_{sc} compared to Li-doped devices. Since we could not find any significant difference both in PIA and TAS, we conclude that the origin of improved fill factor can be directly correlated to a reduced series resistance, which can be achieved by utilizing PIL-doping of the organic semiconductor.

■ CONCLUSIONS

In summary, we have reported a new p-doping mechanism, which is compatible with solution processing of organic semiconductors in air or in inert atmosphere. The conductivity of OS films significantly improves if PILs are added to the solution. In particular, we show that H-TFSI increases the conductivity of spiro-OMeTAD by 3 orders of magnitude. We demonstrate that H-TFSI promotes spiro-OMeTAD single electron oxidation and thus effective p-doping in the semiconducting film. We describe a general PIL-doping mechanism that "consumes" electrons, leaving free holes on the organic matrix. Although in this work we report data only for spiro-OMeTAD, we have observed PIL-doping in poly(3-hexylthiophene), poly (*N*,*N*-diphenyl-4-methoxyphenylamine-4′,4″-diyl), and sexthiophene (more details to follow in a subsequent publication).

Exemplifying these concepts, we demonstrate hybrid solar cells, both ss-DSSCs and MSSCs, with improved PCE compared to the state-of-the-art. Particularly, we replace the commonly used additive composition, Li-TFSI and *t*BP, with a single PIL. We use photovoltage−photocurrent decay and PIA to establish that the significantly improved device performance is attributed to reduced charge transport resistance in the hole-transporting matrix potentiated by PIL-doping.

■ EXPERIMENTAL SECTION

Doping Procedure. The doping procedure was carried out under inert atmosphere (oxygen and water free). Chlorobenzene and acetonitrile were purchased from Sigma-Aldrich in reagent and anhydrous grades. Before introducing the solvents into an oxygen- and water-free glovebox environment, they were deaerated by bubbling with dry nitrogen for several hours. Spiro-OMeTAD was purchased from Lumetec and the dopants (H-TFSI, Li-TFSI, Himi-TFSI, and Et_4N-TFSI) from Sigma-Aldrich. All the chemicals were purchased in their highest available purity and were used without further purification. They have been delivered sealed in inert atmosphere and were opened and stored directly in a glovebox. In particular, H-TFSI is highly sensitive to the air moisture, and just a few minutes of air exposure could significantly hydrate it. Then, a 90 mM solution of spiro-OMeTAD in chlorobenzene was prepared by stirring the mixture overnight at 70 °C. Solutions of ionic liquids (H-TFSI, Himi-TFSI, and Et_4N-TFSI) and Li-TFSI in acetonitrile have been prepared by varying the concentration in order to add always the same volume (1/10 of the final volume) of dopant solution (in acetonitrile) to the spiro-OMeTAD solution (in chlorobenzene). The solution spiro-OMeTAD plus dopant (acetonitrile/chlorobenzene 1/10 v/v) was left stirring at 120 °C overnight in a glovebox. After cooling to room temperature, the solution was filtered using a PTFE membrane of pore size 0.2 μm (Aldrich). Where appropriate, *t*BP was added (10 μL each mL of solution) immediately before spin coating the solution onto the substrate.

Conductivity Measurements. Spiro-OMeTAD solutions with various amounts of dopant were spin coated at 2000 rpm onto a mesoporous SiO_2 layer prepared on glass slides (particle size 40 nm, mesoporous layer thickness 300 nm) and were dried at 140 °C for 30 min in inert atmosphere. Silver contacts (150 nm thick) were applied via thermal evaporation through a shadow mask in 2×10^{-6} Torr vacuum. The electrode pattern was designed for four point probe measurements with a force channel length (direction of current flow) of 1 mm and a width of 1 cm and a sense channel length of 300 μm and width of 1 mm. The J−V characteristics of these samples were collected at room temperature with a Keithley 2420 source meter unit to extract both the bulk and the contact resistance.[75] The contact resistance was found to be negligible compared to the bulk at each doping level. All the samples were prepared and measured under inert atmosphere and with filtered UV light. No relevant visible light dependence of conductivity was observed.

UV−vis Spectra. The sample preparation was identical to the devices for conductivity measurements with the exception that no silver electrodes were deposited on the top of the sample. All the samples were prepared in inert atmosphere and in filtered UV light. Absorbance measurements of the films were taken in air (∼1 min air exposure) using a commercial spectrophotometer (Varian Cary 300 UV−vis, U.S.A.). Baseline measurements were performed on mesoporous SiO_2 substrate without spiro-OMeTAD.

NMR. ^{1}H NMR spectra were recorded on a Bruker Advance 500 spectrometer (500 MHz). Anhydrous deuterated dimethyl sulfoxide was used as solvent, and chemical shifts, δ, are given in ppm, using the solvent residual signal as the internal standard. The samples were prepared in inert atmosphere, and the spectra were collected immediately after the preparation. A complete signal quenching of spiro-OMeTAD was observed after a solution of spiro-OMeTAD and Himi-TFSI was left for ∼3 h (see Table 4).

Table 4. ^{1}H NMR Chemical Shift of Significant Peaks

Himi-TFSI	spiro-OMeTAD	spiro-OMeTAD + Himi-TFSI (30 mol %)
8.75 (s, 1H)		9.66 (s, 1H)
	6.91−6.73 (m, 32H)	6.95−6.87 (m, 0.1H)
	6.69 (d, J = 1.6 Hz, 2H); 6.67 (d, J = 1.7 Hz, 2H)	6.85−6.75 (m, 0.5H)
4.20−4.12 (m, 2H)		4.24 (t, J = 7.4 Hz, 2H)
3.94 (s, 3H)		4.03 (s, 3H)
	3.70 (s, 24H)	3.80−3.75 (m, 1H)
1.93−1.78 (m, 2H)		1.96−1.75 (m)
1.38−1.22 (m, 6H)		1.39−1.21 (m, 6H)
0.88 (t, J = 6.9 Hz, 3H)		0.89 (t, J = 6.7 Hz, 3H)

Himi-TFSI: 8.75 (s, 1H); 7.32 (t, J = 1.7 Hz, 1H); 7.29 (t, J = 1.7 Hz, 1H); 4.20−4.12 (m, 2H); 3.94 (s, 3H); 1.93−1.78 (m, 2H); 1.38−1.22 (m, 6H); 0.88 (t, J = 6.9 Hz, 3H).

spiro-OMeTAD: 7.46 (d, J = 8.4 Hz, 4H); 6.91−6.73 (m, 32H); 6.69 (d, J = 1.6 Hz, 2H); 6.67 (d, J = 1.7 Hz, 2H); 6.17 (d, J = 1.9 Hz, 4H); 3.70 (s, 24H).

spiro-OMeTAD + Himi-TFSI (30 mol %): 9.66 (s, 1H); 7.40−7.19 (m, 4H); 6.95−6.87 (m, 0.1H); 6.85−6.75 (m, 0.5H); 4.24 (t, J = 7.4 Hz, 2H); 4.03 (s, 3H), 3.80−3.75 (m, 1H); 1.96−1.75 (m, ?H); 1.39−1.21 (m, 6H); 0.89 (t, J = 6.7 Hz, 3H).

Computational Details. The molecular structure of both the protonated and the nonprotonated species was optimized using the B3LYP[76−78] as the exchange−correlation functional and 6-31G** as the basis set[79,80] both in vacuum and in solution by including the solution effects through a conductor-like polarizable continuum model (C-PCM)[81−84] with ethanol as the solvent. We used the same computational level employed in a previous report by Fantacci et al.,[33] even though in the present study all the reported calculations were performed using the Gaussian 09 program package.[33] The electronic structure of the investigated species was briefly analyzed. To evaluate the oxidation potential of the investigated species, we used the rigorous calculation of the Gibbs free energy difference between the neutral and the oxidized species (see the report from Oligaro et al.[85] for details); concisely, the Gibbs free energy in solution (G^{i}_{sol}) of the oxidized and the reduced species are computed by adding the Gibbs energy in vacuum (G^{i}_{vac}) (obtained by including the vibrational contribution to the partition function) to the energy of solvation of the given species (ΔG_{solv}).

EPR Analysis. The sample was measured using an X-band (9 GHz) Bruker Elexys E-500 spectrometer (Bruker, Rheinstetten, Germany). Capillaries containing the samples were placed in a standard 4 mm quartz sample tube. The temperature of the sample was regulated to and maintained at 25 °C throughout the measurement by passing thermostatic nitrogen gas through a quartz Dewar. The instrument settings used were sweep width, 100 G; resolution, 1024 points; modulation frequency, 100 kHz; modulation amplitude, 1.0 G; time constant, 20.5 ms. The EPR spectrum was measured with an attenuation of 10 dB (~20 mW) to avoid microwave saturation of the resonance absorption curve. Numerous scans, typically 16, were accumulated to improve the signal-to-noise ratio. The spectral parameters calculated from this averaged spectrum are summarized in Table 5.

Table 5. EPR Spectral Parameters for Spiro-OMeTAD Doped with H-TFSI

	spiro-OMeTAD−H-TFSI
g-factor	2.0032 ± 0.0004
$\Delta B(G)$	4.6 ± 0.2
spin g^{-1}	8.4×10^{6}

The *g*-factor was determined by using an internal standard to provide an exact position of the EPR signal. The standard was an ethanol solution of 4-hydroxy-TEMPO.[42] This solution was introduced into the EPR tube, where a capillary containing spiro-OMeTAD powder was also added in order to measure the corresponding spectrum.

ss-DSSCs Fabrication. ss-DSSCs were prepared according to the previous method.[34] All solvents used for device fabrication were reagent and anhydrous grade. FTO substrates (7 Ω/sq, Pilkington, U.S.A.) were etched with zinc powder and 2 M aqueous HCl to give the desired electrode patterning. The substrates were cleaned with Hellmanex (2% by volume in water, Aldrich), deionized water, acetone, and ethanol. Remaining organic residues were removed with 10 min of oxygen plasma cleaning. The FTO sheets were subsequently coated with a compact layer of TiO_2 (~75 nm) by aerosol spray pyrolysis deposition at 275 °C, using oxygen as the carrier gas. Films of 1.5 μm thick mesoporous TiO_2 were then deposited by screen printing a commercial paste (Dyesol 18NR-T). The TiO_2 films were gradually heated to 500 °C and sintered for 30 min in air. Once cooled, the samples were immersed into a 15 mM $TiCl_4$ aqueous solution for 45 min at 70 °C and then sintered at 500 °C for 45 min. After cooling to 70 °C, the substrates were immersed in a 500 μM dye solution, in a 1:1 mixture of acetonitrile and *tert*-butyl alcohol by volume, for 1 h. The dye used in this study was D102, previously reported by Horiushi et al.[49] After the dyed films were rinsed in acetonitrile, the spiro-OMeTAD was applied by spin coating at 1000 rpm for 45 s in air from a solution prepared as previously described. After drying overnight, 150 nm silver back electrode contacts were applied by thermal evaporation.

MSSCs Fabrication. MSSCs were prepared according to the previous method.[26] All solvents used for device fabrication were reagent and anhydrous grade. FTO substrates (7 Ω/sq, Pilkington US) were etched with zinc powder and 2 M aqueous HCl to give the desired electrode patterning. The substrates were cleaned with Hellmanex (2% by volume in water, Aldrich), deionized water, acetone, and ethanol. Remaining organic residues were removed with 10 min of oxygen plasma cleaning.The FTO sheets were subsequently coated with a compact layer of TiO_2 (~75 nm) by aerosol spray pyrolysis deposition at 270 °C, using oxygen as the carrier gas. The TiO_2 films were gradually heated to 500 °C and sintered for 30 min in air. Once cooled, 400 nm thick films of mesoporous Al_2O_3 were deposited on the top of the compact TiO_2 layer by spin coating an Aldrich isopropanol dispersion of 40 nm Al_2O_3 particles. The substrates were heated to 150 °C for 30 min and then cooled to room temperature. Then, perovskite crystals ABX_3 (A = CH_3NH_3, B = Pb, and X = I_{1-x}, Cl_x) were deposited according to the procedure previously reported.[25] The spiro-OMeTAD was applied by spin coating at 2000 rpm for 45 s in air from a solution prepared as previously described. After drying overnight, 150 nm silver back electrode contacts were applied by thermal evaporation.

Photovoltage and Photocurrent Decay. Measurements were performed by a similar method to O′Regan et al. and as described elsewhere.[61,86,87] All devices were stored in air and in dark for 72 h prior to testing.

Photoinduced Absorption Spectroscopy (PIA). The films were excited with monochromatic light (496.5 nm) at a power density of 50 mW cm^{-2}, modulated with a chopper at 23 Hz. White light from a halogen lamp was used as a probe. After passing through a monochromator (Princeton Instruments, SP2300), the signal was detected with an amplified Si diode in the visible (Thorlabs, PDA10A) and InGaAs (Acton Research Coproration, ID-441-C) in the near-infrared. Signals were acquired with a lock-in (Stanford Research Systems, SRS830) and an acquisition module (National instruments, USB-6008). The instrument was controlled with National Instruments LabView software. Samples were prepared according to the fabrication procedure described for ss-DSSCs in the previous paragraph.

Transient Absorption Spectroscopy (TAS). Pulsed excitation (λ_{ex} = 500 nm, 7 ns pulse duration, 10 Hz repetition rate) of the dyed film was performed using an Nd:YAG laser (Ekspla, NT340) with a laser fluence on the sample maintained at <50 μJ cm^{-2} per pulse. The probe light, generated by a continuous-wave xenon arc lamp, was first passed through a monochromator (Acton Research Corporation, SpectraPro- 2150i), various optical elements, the sample, and then through a second monochromator (Acton Research Corporation, SpectraPro-2300i) before being detected in the visible region by a fast photomultiplier tube module biased with 750 V (Hamamatsu, R9110). In the NIR, detection utilized a fast diode (Thorlabs, SM05PD5A). Signals were recorded on an oscilloscope (Tektronix, DPO3054). Satisfactory signal-to-noise ratios were typically obtained by averaging 256 laser pulses. The data was smoothed with a Savitsky−Golay algorithm for presentation. Samples were prepared according to the fabrication procedure described for ss-DSSCs in the previous paragraph.

Photovoltaic Characterization.[65] For measuring device merit parameters, simulated AM 1.5 sunlight was generated with a class AAB ABET solar simulator calibrated to AM1.5, 100 mW cm^{-2} irradiance, using an NREL-calibrated KG5 filtered silicon reference cell, with <1% mismatch factor; the current−voltage curves were recorded with a sourcemeter (Keithley 2400, USA). The solar cells were masked with a metal mask defining the active area (0.08 cm^2) of the solar cells. MSSCs were measured immediately after the thermal evaporation of electrodes.

■ ASSOCIATED CONTENT

Supporting Information

Himi-TFSI doped spiro-OMeTAD UV−vis absorption; spiro-OMeTAD ^{1}H NMR in deuterated dimethyl sulfoxide; optimized structures of spiro-OMeTAD protonated species and relative formation energies; EPR spectrum of undoped spiro-OMeTAD; TAS; device cross-section scanning electron microscopy image. This information is available free of charge via the Internet at http://pubs.acs.org.

■ AUTHOR INFORMATION

Corresponding Author
h.snaith1@physics.ox.ac.uk

Present Address
[#]Laboratory of Photonics and Interfaces, Institute of Chemical Sciences and Engineering, École polytechnique fédérale de Lausanne (EPFL), Station 6, CH-1015 Lausanne, Switzerland

Notes

The authors declare no competing financial interest.

■ ACKNOWLEDGMENTS

This work was funded by the Engineering and Physical Sciences Research Council (EPSRC) APEX project and the European Commission, under the SANS project, grant agreement no. 246124.

■ REFERENCES

(1) Mei, J.; Diao, Y.; Appleton, A. L.; Fang, L.; Bao, Z. *J. Am. Chem. Soc.* **2013**, *135*, 6724.

(2) Chiang, C.; Fincher, C., Jr; Park, Y.; Heeger, A.; Shirakawa, H.; Louis, E.; Gau, S.; MacDiarmid, A. G. *Phys. Rev. Lett.* **1977**, *39*, 1098.

(3) MacDiarmid, A. G. *Angew. Chem., Int. Ed.* **2001**, *40*, 2581.

(4) MacDiarmid, A. G.; Heeger, A. J. *Synth. Met.* **1980**, *1*, 101.

(5) Han, C.; Elsenbaumer, R. *Synth. Met.* **1989**, *30*, 123.

(6) dos Santos, D.; Galvão, D.; Laks, B. *Solid State Commun.* **1990**, *74*, 215.

(7) Spangler, C. W.; Bryson, P.; Liu, P. K.; Dalton, L. R. *J. Chem. Soc., Chem. Commun.* **1992**, 253.

(8) Hu, B.; Zhu, X.; Chen, X.; Pan, L.; Peng, S.; Wu, Y.; Shang, J.; Liu, G.; Yan, Q.; Li, R. W. *J. Am. Chem. Soc.* **2012**, *134* (42), 17408−17411.

(9) Nam, S.; Kim, J.; Lee, H.; Kim, H.; Ha, C.-S.; Kim, Y. *ACS Appl. Mater. Interfaces* **2012**, *4*, 1281.

(10) Zhu, X. Q.; Zhang, M. T.; Yu, A.; Wang, C. H.; Cheng, J. P. *J. Am. Chem. Soc.* **2008**, *130*, 2501.

(11) Wei, P.; Oh, J. H.; Dong, G.; Bao, Z. *J. Am. Chem. Soc.* **2010**, *132*, 8852.

(12) Wren, S. W.; Vogelhuber, K. M.; Garver, J. M.; Kato, S.; Sheps, L.; Bierbaum, V. M.; Lineberger, W. C. *J. Am. Chem. Soc.* **2012**, *134*, 6584.

(13) Burschka, J.; Dualeh, A.; Kessler, F.; Baranoff, E.; Cevey-Ha, N. L.; Yi, C.; Nazeeruddin, M. K.; Grätzel, M. *J. Am. Chem. Soc.* **2011**, *133* (45), 18042−18045.

(14) DAndrade, B. W.; Forrest, S. R.; Chwang, A. B. *Appl. Phys. Lett.* **2003**, *83*, 3858.

(15) Pfeiffer, M.; Leo, K.; Zhou, X.; Huang, J. S.; Hofmann, M.; Werner, A.; Blochwitz-Nimoth, J. *Org. Electron.* **2003**, *4*, 89.

(16) Leijtens, T.; Ding, I. K.; Giovenzana, T.; Bloking, J. T.; McGehee, M. D.; Sellinger, A. *ACS Nano* **2012**, *6* (2), 1455−1462.

(17) Snaith, H. J.; Zakeeruddin, S. M.; Wang, Q.; Péchy, P.; Grätzel, M. *Nano Lett.* **2006**, *6*, 2000.

(18) Shen, Y.; Hosseini, A. R.; Wong, M. H.; Malliaras, G. G. *ChemPhysChem* **2004**, *5*, 16.

(19) Kruger, J.; Plass, R.; Cevey, L.; Piccirelli, M.; Gratzel, M.; Bach, U. *Appl. Phys. Lett.* **2001**, *79*, 2085.

(20) Blochwitz, J.; Fritz, T.; Pfeiffer, M.; Leo, K.; Alloway, D. M.; Lee, P. A.; Armstrong, N. R. *Org. Electron.* **2001**, *2*, 97.

(21) Riede, M.; Uhrich, C.; Widmer, J.; Timmreck, R.; Wynands, D.; Schwartz, G.; Gnehr, W. M.; Hildebrandt, D.; Weiss, A.; Hwang, J. *Adv. Funct. Mater.* **2011**, *21*, 3019−3028.

(22) Greaves, T. L.; Drummond, C. J. *Chem. Rev. (Washington, DC, U. S.)* **2008**, *108*, 206.

(23) Margaretta, E.; Olmeda, C.; Yu, L. *J. Appl. Polym. Sci.* **2013**, *127*, 2453.

(24) Bach, U.; Lupo, D.; Comte, P.; Moser, J.; Weissörtel, F.; Salbeck, J.; Spreitzer, H.; Grätzel, M. *Nature* **1998**, *395*, 583.

(25) Lee, M. M.; Teuscher, J.; Miyasaka, T.; Murakami, T. N.; Snaith, H. J. *Science* **2012**, *338*, 643.

(26) Ball, J. M.; Lee, M. M.; Hey, A.; Snaith, H. *Energy Environ. Sci.* **2013**, *6*, 1739−1743.

(27) Abate, A.; Petrozza, A.; Roiati, V.; Guarnera, S.; Snaith, H.; Matteucci, F.; Lanzani, G.; Metrangolo, P.; Resnati, G. *Org. Electron.* **2012**, *13* (11), 2474−2478.

(28) Abate, A.; Petrozza, A.; Cavallo, G.; Lanzani, G.; Matteucci, F.; Bruce, D. W.; Houbenov, N.; Metrangolo, P.; Resnati, G. *J. Mater. Chem. A* **2013**, *1*, 6572.

(29) Armand, M.; Endres, F.; MacFarlane, D. R.; Ohno, H.; Scrosati, B. *Nat. Mater.* **2009**, *8*, 621.

(30) Yu, L.; Pizio, B. S.; Vaden, T. D. *J. Phys. Chem. B* **2012**, *116*, 6553−6560.

(31) Fevre, M. v.; Pinaud, J.; Leteneur, A.; Gnanou, Y.; Vignolle, J.; Taton, D.; Miqueu, K.; Sotiropoulos, J.-M. *J. Am. Chem. Soc.* **2012**, *134*, 6776.

(32) Ott, L. S.; Cline, M. L.; Deetlefs, M.; Seddon, K. R.; Finke, R. G. *J. Am. Chem. Soc.* **2005**, *127*, 5758.

(33) Fantacci, S.; De Angelis, F.; Nazeeruddin, M. K.; Grätzel, M. *J. Phys. Chem. C* **2011**, *91* (2), 192−198.

(34) Abate, A.; Leijtens, T.; Pathak, S.; Teuscher, J.; Avolio, R.; Errico, M. E.; Kirkpatrik, J.; Ball, J. M.; Docampo, P.; McPherson, I. *Phys. Chem. Chem. Phys.* **2013**, *15*, 2572.

(35) Gregg, B. A.; Chen, S. G.; Cormier, R. A. *Chem. Mater.* **2004**, *16*, 4586.

(36) Bertini, I.; Luchinat, C.; Parigi, G. *Solution NMR of paramagnetic molecules: applications to metallobiomolecules and models*; Elsevier Science: Amsterdam, 2001; Vol. 2.

(37) Yoder, J. C.; Roth, J. P.; Gussenhoven, E. M.; Larsen, A. S.; Mayer, J. M. *J. Am. Chem. Soc.* **2003**, *125*, 2629.

(38) Uğurbil, K.; Mitra, S. *Proc. Natl. Acad. Sci. U.S.A.* **1985**, *82*, 2039.

(39) Jensen, M. R.; Hansen, D. F.; Led, J. J. *J. Am. Chem. Soc.* **2002**, *124*, 4093.

(40) Goez, M.; Frisch, I.; Sartorius, I. *Beilstein J. Org. Chem.* **2013**, *9*, 437.

(41) Lungwitz, R.; Spange, S. *ChemPhysChem* **2012**, *13*, 1910.

(42) Alvarez, F. J. D.; Orelle, C.; Davidson, A. L. *J. Am. Chem. Soc.* **2010**, *132*, 9513.

(43) She, C.; Anderson, N. A.; Guo, J.; Liu, F.; Goh, W.-H.; Chen, D.-T.; Mohler, D. L.; Tian, Z.-Q.; Hupp, J. T.; Lian, T. *J. Phys. Chem. B* **2005**, *109*, 19345.

(44) Krüger, J.; Plass, R.; Cevey, L.; Piccirelli, M.; Grätzel, M.; Bach, U. *Appl. Phys. Lett.* **2001**, *79*, 2085.

(45) Katz, M. J.; Vermeer, M. J. D.; Farha, O. K.; Pellin, M. J.; Hupp, J. T. *Langmuir* **2012**, *29* (2), 806−814.

(46) Cappel, U. B.; Smeigh, A. L.; Plogmaker, S.; Johansson, E. M. J.; Rensmo, H.; Hammarström, L.; Hagfeldt, A.; Boschloo, G. *J. Phys. Chem. C* **2011**, *115* (10), 4345−4358.

(47) Cappel, U. B.; Daeneke, T.; Bach, U. *Nano Lett.* **2012**, *12* (9), 4925−4931.

(48) Li, Y.-F.; Selloni, A. *J. Am. Chem. Soc.* **2013**, *135* (24), 9195−9199.

(49) Horiuchi, T.; Miura, H.; Uchida, S. *Chem. Commun.* **2003**, 3036.

(50) Schmidt-Mende, L.; Bach, U.; Humphry-Baker, R.; Horiuchi, T.; Miura, H.; Ito, S.; Uchida, S.; Grätzel, M. *Adv. Mater.* **2005**, *17*, 813.

(51) Barnes, P. R.; Miettunen, K.; Li, X.; Anderson, A. Y.; Bessho, T.; Gratzel, M.; O'Regan, B. C. *Adv. Mater.* **2013**, *25*, 1881−1922.

(52) Sivaram, V.; Kirkpatrick, J.; Snaith, H. *J. Appl. Phys.* **2013**, *113*, 063709.
(53) Fabregat-Santiago, F.; Mora-Seró, I.; Garcia-Belmonte, G.; Bisquert, J. *J. Phys. Chem. B* **2003**, *107*, 758.
(54) Leijtens, T.; Lim, J.; Teuscher, J.; Park, T.; Snaith, H. J. *Adv. Mater.* **2013**, *25*, 3227−3233.
(55) Wang, H.; Peter, L. M. *J. Phys. Chem. C* **2009**, *113*, 18125.
(56) Schröder, C.; Wakai, C.; Weingärtner, H.; Steinhauser, O. *J. Chem. Phys.* **2007**, *126*, 084511.
(57) Fredin, K.; Nissfolk, J.; Boschloo, G.; Hagfeldt, A. *J. Electroanal. Chem.* **2007**, *609*, 55.
(58) Koops, S. E.; O'Regan, B. C.; Barnes, P. R. F.; Durrant, J. R. *J. Am. Chem. Soc.* **2009**, *131*, 4808.
(59) Pu, P.; Cachet, H.; Laidani, N.; Sutter, E. *J. Phys. Chem. C* **2012**, *116*, 22139.
(60) Abrusci, A.; Santosh Kumar, R. S.; Al-Hashimi, M.; Heeney, M.; Petrozza, A.; Snaith, H. J. *Adv. Funct. Mater.* **2011**, *21*, 2571.
(61) O'Regan, B.; Xiaoe, L.; Ghaddar, T. *Energy Environ. Sci.* **2012**, *5*, 7203.
(62) Kopidakis, N.; Benkstein, K. D.; van de Lagemaat, J.; Frank, A. J. *J. Phys. Chem. B* **2003**, *107*, 11307.
(63) Greiner, M. T.; Helander, M. G.; Tang, W. M.; Wang, Z. B.; Qiu, J.; Lu, Z. H. *Nat. Mater.* **2011**, *11*, 76−81.
(64) Cappel, U. B.; Plogmaker, S.; Johansson, E. M.; Hagfeldt, A.; Boschloo, G.; Rensmo, H. *Phys. Chem. Chem. Phys.* **2011**, *13*, 14769.
(65) Snaith, H. J. *Energy Environ. Sci.* **2012**, *5*, 6513.
(66) Kelly, C. A.; Farzad, F.; Thompson, D. W.; Stipkala, J. M.; Meyer, G. J. *Langmuir* **1999**, *15*, 7047.
(67) Lunell, S.; Stashans, A.; Ojamäe, L.; Lindström, H.; Hagfeldt, A. *J. Am. Chem. Soc.* **1997**, *119*, 7374.
(68) Kim, J.-Y.; Kim, J. Y.; Lee, D.-K.; Kim, B.; Kim, H.; Ko, M. J. *J. Phys. Chem. C* **2012**, *116*, 22759.
(69) Nicolai, H.; Kuik, M.; Wetzelaer, G.; de Boer, B.; Campbell, C.; Risko, C.; Brédas, J.; Blom, P. *Nat. Mater.* **2012**, *11*, 882.
(70) Boschloo, G.; Hagfeldt, A. *Inorg. Chim. Acta* **2008**, *361*, 729.
(71) Ardo, S.; Sun, Y.; Castellano, F. N.; Meyer, G. J. *J. Phys. Chem. B* **2010**, *114*, 14596.
(72) Ardo, S.; Sun, Y.; Staniszewski, A.; Castellano, F. N.; Meyer, G. J. *J. Am. Chem. Soc.* **2010**, *132*, 6696.
(73) Gal, J.-F.; Maria, P.-C.; Decouzon, M.; Mó, O.; Yáñez, M.; Abboud, J. L. M. *J. Am. Chem. Soc.* **2003**, *125*, 10394.
(74) Canesi, E. V.; Binda, M.; Abate, A.; Guarnera, S.; Moretti, L.; D'Innocenzo, V.; Kumar, R. S. S.; Bertarelli, C.; Abrusci, A.; Snaith, H. *Energy Environ. Sci.* **2012**, *5*, 9068.
(75) Planells, M.; Abate, A.; Hollman, D. J.; Stranks, S. D.; Bharti, V.; Gaur, J.; Mohanty, D.; Chand, S.; Snaith, H.; Robertson, N. *J. Mater. Chem. A* **2013**, *1*, 6949−6960.
(76) Becke, A. D. *J. Chem. Phys.* **1993**, *98*, 5648.
(77) Lee, C.; Yang, W.; Parr, R. G. *Phys. Rev. B* **1988**, *37*, 785.
(78) Miehlich, B.; Savin, A.; Stoll, H.; Preuss, H. *Chem. Phys. Lett.* **1989**, *157*, 200.
(79) Rassolov, V. A.; Ratner, M. A.; Pople, J. A.; Redfern, P. C.; Curtiss, L. A. *J. Comput. Chem.* **2001**, *22*, 976.
(80) Rassolov, V. A.; Pople, J. A.; Ratner, M. A.; Windus, T. L. *J. Chem. Phys.* **1998**, *109*, 1223.
(81) Tomasi, J.; Mennucci, B.; Cammi, R. *Chem. Rev. (Washington, DC, U. S.)* **2005**, *105*, 2999.
(82) Scalmani, G.; Frisch, M. J.; Mennucci, B.; Tomasi, J.; Cammi, R.; Barone, V. *J. Chem. Phys.* **2006**, *124*, 094107.
(83) Improta, R.; Scalmani, G.; Frisch, M. J.; Barone, V. *J. Chem. Phys.* **2007**, *127*, 074504.
(84) Improta, R.; Barone, V.; Scalmani, G.; Frisch, M. J. *J. Chem. Phys.* **2006**, *125*, 054103.
(85) Ogliaro, F.; Bearpark, M.; Heyd, J.; Brothers, E.; Kudin, K.; Staroverov, V.; Kobayashi, R.; Normand, J.; Raghavachari, K.; Rendell, A. Wallingford, CT, 2009.
(86) Docampo, P.; Guldin, S.; Stefik, M.; Tiwana, P.; Orilall, M. C.; Hüttner, S.; Sai, H.; Wiesner, U.; Steiner, U.; Snaith, H. J. *Adv. Funct. Mater.* **2010**, *20*, 1787.
(87) Bisquert, J.; Zaban, A.; Greenshtein, M.; Mora-Seró, I. *J. Am. Chem. Soc.* **2004**, *126*, 13550.